Available online at www.sciencedirect.com
ScienceDirect
Ceramics International 38 (2012) 775–786
CERAMICS INTERNATIONAL
www.elsevier.com/locate/ceramint

A factorial design approach for pressureless sintering in air of (Pb,La)(Zr,Ti)O_3 synthesized via coprecipitation of oxide–alkoxides

Ray Gunawidjaja, Thandar Myint, Hergen Eilers *

Applied Sciences Laboratory, Institute for Shock Physics, Washington State University, Spokane, WA 99210-1495, USA

Received 9 May 2011; received in revised form 10 July 2011; accepted 1 August 2011
Available online 24th August 2011

Abstract

Using factorial design for guidance, (Pb,La)(Zr,Ti)O_3 (PLZT) ceramics of compositions 9.5/65/35 and 5/Z/T (Z/T = 60/40, 54/46, 40/60) were pressureless sintered in air. Theoretical bulk densities of up to 96% were achieved. The starting materials were obtained from the coprecipitation of the oxide–alkoxides. The relevant sintering parameters were initially screened with the 9.5/65/35 composition using a factorial design method to achieve high-density, high purity perovskite-phase, and small grain-size. The variables were ball-milling time, cold-press pressure, sintering time, sintering temperature, vacuum treatment, and PLZT to $PbZrO_3$ weight ratio. The optimized sintering conditions were then applied to the remaining PLZT compositions, as well as to a commercially purchased PLZT powder, PLZT 8/40/60 to yield similar ceramic qualities. The ceramic samples were characterized with SEM, XRD, and Raman spectroscopy, and their relative permittivity, ε_r, and the piezoelectric constant, d_{33}, were measured.

Keywords: A. Sintering; C. Piezoelectric properties; C. Impedance; C. Optical properties; D. PLZT

1. Introduction

(Pb,La)(Zr,Ti)O_3 (PLZT) is a well-known ceramic material that, depending on its composition, exhibits a wide range of properties at room temperature, including ferroelectricity, antiferroelectricity, pyroelectricity, and paraelectricity [1]. In order to fully utilize these unique properties, a high density, single perovskite phase, and small grain-size are desired. These properties are usually achieved with pressure-assisted sintering in the presence of a combustible oxygen environment [2]. Nevertheless, pressureless sintering in air has been demonstrated [1,3,4]. This technique is low-cost, facile, and contamination free (no hot-pressing die materials needed), and is favored to achieve high-densities in thin pellets (<0.5 mm), because the densification process initiates from the exterior [4]. Thin PLZT ceramics are favored in opaque photostrictive devices in which photons can only interact with the material near the surface. Poosanaas et al. determined that an optimum PLZT ceramic thickness for such application is 33 μm [5]. To achieve shrinkage in the interior, hot-pressing or vacuum sintering is employed [6,7]. In addition, the amount of pores can be minimized by vigorous ball-milling or by synthesizing a fine (nanoscale) sized powder precursor [8,9].

Another critical issue for achieving high-density PLZT ceramics is the volatilization of PbO during sintering above the melting point of PbO (888 °C). This volatilization leaves behind lattice vacancies resulting in poor microstructures and nonstoichiometric compositions [4]. PLZT sintering at elevated temperature is thus categorized as sintering with reactive liquids. The elevated temperature is necessary for an appreciable solubility of the solid in the liquid. PLZT is more easily sintered compared to PZT compounds because the additional La_2O_3 increases the solubility of $PbZrO_3$ and $PbTiO_3$. In an oxygen-rich sintering environment, oxygen-filled pores easily disappear by migration of oxygen via lattice diffusion [10]. Furthermore, the effects of volatilization of PbO can be overcome by either adding excess stoichiometric amounts of PbO in the green ceramic precursor or by surrounding the PLZT ceramics with suitable Pb-containing powders to maintain a PbO-rich atmosphere during the sintering process [10].

It is worth noting that for the same sintering parameters the obtained ceramic density depends on the method by which the PLZT powder is synthesized [11–13]. The PLZT powder

* Corresponding author. Tel.: +1 509 358 7681; fax: +1 509 358 7728.
E-mail address: Eilers@wsu.edu (H. Eilers).

0272-8842/$36.00
doi:10.1016/j.ceramint.2011.08.004

employed in this work was synthesized via coprecipitation of oxide–alkoxides (see Section 2). The use of liquid precursors in this process substantially reduces non-stoichiometry and wide fluctuation in compositions, as well as poor microstructure that is often encountered in the conventional mixed oxide process [1]. In a typical oxide–alkoxide coprecipitation process, the liquid precursors are mixed in the desired proportions, reacted, and then coprecipitated from solutions.

While pressureless air–atmosphere sintering has been demonstrated in the literatures, the accounts usually focus on a particular composition and involve the conventional mixed oxide process [1,3,4,12]. In this work, we employ the factorial design approach to systematically screen out the factors that are critical to yielding a high-density single-perovskite-phase PLZT specimen from coprecipitated oxide–alkoxides PLZT powder. We are using a simple sintering setup and pressureless sintering in air of uniaxially pressed green bodies. Because of the numerous reports on PLZT L/65/35 available in the scientific literature, our initial work focuses on PLZT 9.5/65/35. This composition is close to the morphotropic phase boundary (MPB), between the rhombohedral and tetragonal phases, and exhibits high piezoelectric coupling [1]. A well-sintered ferroelectric PLZT 9.5/65/35 ceramic is optically transparent. A high-density and high-transparency PLZT sample translates into good electro-optical properties that make them useful for optical memory applications [2]. We then applied the determined optimized sintering conditions to various PLZT compositions across the MPB (5/60/40, 5/54/46, and 5/40/60), as well as to a commercially purchased PLZT 8/40/60 powder (Praxair, Inc.).

2. Experimental and methods

Lead (II) oxide (99.99%) and lanthanum (II) acetate sesquihydrate (99.99%) were purchased from Alfa-Aesar. Zirconium (IV) butoxide solution in 1-butanol (80 wt%), tetrabutyl orthotitanate (≥97%) and lead (II) zirconate powder (99%) were bought from Aldrich, Inc. PLZT samples were prepared following the procedures described in the literature [14]. The molar composition of PLZT was adjusted according to La/Zr/Ti mole ratios of 9.5/65/35, 5/60/40, 5/54/46, and 5/40/60. For comparison, PLZT 8/40/60 powder was purchased from Praxair, Inc.

To obtain about 25 g of calcined PLZT powder, zirconium butoxide, tetrabutyl orthotitanate, and lead oxide in isopropanol (25 wt%) were mixed in an explosion resistant Waring blender (*Caution!* zirconium butoxide, tetrabutyl orthotitanate, and isopropanol are combustible liquids). The mixture was blended for 1 min before an aqueous solution of lanthanum acetate (1:10 water to isopropanol volume ratio) was introduced during blending through a drilled opening in the polycarbonate cover of the blender. The mixture was allowed to blend for 15 min. The solution underwent an exothermic reaction that caused the flask to heat up. The final suspension shows a moccasin appearance. The slurry was then poured into Pyrex® petri dishes, and isopropanol and water were evaporated. The dried cake was easily crushed into powders and calcined at 500 °C for 16 h. 10 g of the calcined powder was wet-milled in a 50 mL Nalgene® bottle with 100 g of yttria-stabilized zirconia (YSZ) balls (3 mm diameter, Inframat Advanced Materials, Inc.) in 20 mL acetone. The milled powder was separated from the YSZ balls by running the mixture through sieves, and the acetone was evaporated. Next, 8 wt% poly(vinyl butyral-co-vinyl alcohol-co-vinyl acetate) binder, Mw 90,000–120,000 (Aldrich, Inc.) was applied to the dried powder via another course of wet-milling (1 h). Without the polymeric binder the PLZT green body does not hold its shape following cold-pressing. For 5 g of the PLZT powder, 50 g of YSZ balls and 15 mL acetone were used. Finally, the powder/binder mixture in acetone was separated from the YSZ balls and the acetone was evaporated. The dried cake was crushed with mortar and pestle, passed through a 25 mesh sieve, and was then ready to use.

Square-shaped green bodies (0.5–1 mm thick) were prepared by pressing about 0.12 mg of the PLZT powder in a square die, length = 6.35 mm (1/4 in.), using a hydraulic press at 30 and 240 MPa for 5 min. The produced green bodies have thicknesses in the 1–1.2 mm range. To remove the organic binder, the green-bodies were rapidly heated to 500 °C at 20 °C/min and then slowly heated between 500 and 800 °C at 1 °C/min. Subsequently, sintering was performed at either 1050 °C or 1250 °C for 2 h or 12 h in a covered alumina crucible [6]. The atmosphere of the chamber was maintained with natural air that was purged at a constant rate of 4 L/min. The chamber pressure was kept constant at 850 Torr (113 Pa). To maintain a sufficient lead atmosphere during the sintering process, the green-bodies were surrounded by lead zirconate powder at certain weight ratios of PLZT green bodies to $PbZrO_3$ powder. Factorial screening was performed (see Section 3). We have employed both full and fractional factorial experiments. In contrast to performing a series of experiments that changes one factor at a time, factorial design requires fewer experimental runs and, if interactions exist between the factors, factorial design accounts for its estimation [15]. In the case of a full factorial experiment, all possible combinations of the levels of the factors are investigated. The total number of runs required in a full factorial experiment for 2-level design is 2^n, where n is the number of factors. Since the number of required runs increases rapidly as the number of factors is increased, we have employed fractional factorial experiment to initially screen the relevant factors, 2^{n-1}. Fractional factorial experiments are done under the assumption that the high-order interaction, i.e. interaction between the factors involved in the experiment, is negligible. It is assumed that the observations are normally and independently distributed with the same variance in each factor level. To verify this assumption, the residual versus predicted plots and normal probability plot of residuals are constructed. The Pareto chart was plotted to identify the factor(s) that significantly affect the experiment [16]. The run order was randomized. For each run, 3 pellet specimens were sintered at once to account for the variation within the single run. The average response of the 3 specimens represents the single run. Each factorial design is un-replicated. Where applicable, the significance level, $\alpha = 0.05$ is used.

The bulk densities of the sintered pellets were estimated using the Archimedes' method. X-ray diffraction spectra were obtained with a PANalytical diffractometer using Cu-K_α radiation, $\lambda = 1.5405$ Å. SEM images were generated with an FEI NOVA-SEM. Each of the sintered PLZT ceramics was poled at 2 kV/mm in 130 °C silicone oil for 15 min. The ceramic pellets were polished with 3 μm diamond paste and gold coated (30 nm) prior to d_{33} and dielectric constant measurements. The d_{33} values were obtained using a piezo d_{33} tester (APC Part #: 90-2030) from APC Products, Inc. The capacitance (C) of the samples was measured at 1 kHz using a HIOKI impedance analyzer (IM 3570). The relative permittivities ε_r of the ceramic pellets were calculated from the measured capacitance (C) using the following formula:

$$\varepsilon_r = \frac{Cd}{\varepsilon_0 A}$$

where C is the capacitance, d is the distance between the electrodes, A is the electrode area, and ε_0 is the permittivity of free space (8.854×10^{-12} F/m). Raman spectra were measured with a home-built Raman setup with 3 cm^{-1} resolution and 532 nm excitation wavelength.

3. Results and discussions

3.1. Screening experiment with half-fraction factorial design

A 2_V^{5-1} factorial experiment was initially performed to screen out the relevant factors affecting the quality of sintered PLZT 9.5/65/35 (Table 1). Considering that the fabrication of dense PLZT ceramics requires highly packed green bodies, minimum PbO loss [17], and preferably to be completed within a short-fabrication time, the following factors were taken into account: (A_1) ball-milling time (4 and 48 h), (B_1) cold-press pressure (30 MPa and 240 MPa), (C_1) sintering time (2 and 12 h), (D_1) sintering temperature (1050 °C and 1250 °C), and (E_1) vacuum treatment (at 1050 °C/30 min). $I = A_1B_1C_1D_1E_1$ was used as the defining relation. The PLZT to $PbZrO_3$ weight is fixed at a ratio of 1:2. The subscript is used to differentiate the factors employed between the three sets of factorial experiments discussed in this work. A good quality PLZT ceramic should have a high density, high purity, and small grain size (<5 μm). Linear shrinkage was measured as a complementary response variable to the ceramic density. The following responses were therefore noted: ceramic density (g/cm^3), grain size (μm), linear shrinkage (%), and relative purity of the perovskite structure.

3.2. PLZT morphology

SEM images of the ceramic surfaces show that the ceramics remain porous following sintering at 1050 °C, which implies that of the three sintering stages, the powders have only undergone the initial stage (Fig. 1 and Table 1) [18]. Density determination using Archimedes' principle is thus inappropriate since the fluid medium could penetrate open pores at the surface. Moreover, the samples are too mechanically fragile – they tend to chip, crack, and crumble – to allow a precise estimation of their bulk density by measuring their mass and dimensions. The ceramics sintered at 1250 °C, however are mechanically robust. These samples have reached the intermediate to final sintering stage, as seen from the lack of pores and the observed grain boundaries. The surface grains are closely packed, as seen from the SEM images (Fig. 1). Sintering of PLZT starts at the exterior of the ceramics, resulting in pores enclosed inside the specimen [4]. Thus, Archimedes' principle can be used to measure the bulk density (Table 3). The intermediate sintering stage is characterized by a drastic decrease in porosity, and hence large shrinkage. The decrease in porosity and shrinkage occurs to a much lesser extent at the final sintering stage. The grain sizes were nonetheless measurable for all samples from their SEM images using the grain-intercept method. The factors

Table 1
A 2_V^{5-1} design for sintering of PLZT (9.5/65/35) ceramics. A_1 = ball-milling (h), B_1 = cold-press pressure (MPa), C_1 = sintering time (h), D_1 = sintering temperature (°C), and E_1 = vacuum treatment (N/Y).

No.	A_1	B_1	C_1	D_1	E_1: $A_1B_1C_1D_1$	Grain size (μm)	I_{ZrO_2}/I_{PLZT} [a]	Pellet quality
1-1	4	30	2	1050	Y	0.32 ± 0.10	0.007	Brittle
1-2	4	30	2	1250	N	1.53 ± 0.10	0.014	Robust
1-3	4	30	12	1050	N	0.42 ± 0.13	0.003	Brittle
1-4	4	30	12	1250	Y	2.67 ± 0.15	0.020	Robust
1-5	4	240	2	1050	N	0.31 ± 0.09	0.008	Brittle
1-6	4	240	2	1250	Y	1.54 ± 0.17	0.006	Robust
1-7	4	240	12	1050	Y	0.44 ± 0.14	0.007	Brittle
1-8	4	240	12	1250	N	2.87 ± 0.09	0.010	Robust
1-9	48	30	2	1050	N	0.28 ± 0.07	0.009	Brittle
1-10	48	30	2	1250	Y	1.60 ± 0.08	0.007	Robust
1-11	48	30	12	1050	Y	0.41 ± 0.13	0.003	Brittle
1-12	48	30	12	1250	N	2.81 ± 0.07	0.011	Robust
1-13	48	240	2	1050	Y	0.32 ± 0.10	0.005	Brittle
1-14	48	240	2	1250	N	1.67 ± 0.07	0.006	Robust
1-15	48	240	12	1050	N	0.45 ± 0.15	0.005	Brittle
1-16	48	240	12	1250	Y	3.10 ± 0.09	0.007	Robust

[a] Peak intensity of XRD spectrum of ZrO_2 at $2\theta = 28.2°$/peak intensity of XRD spectrum of PLZT at $2\theta = 31.4°$.

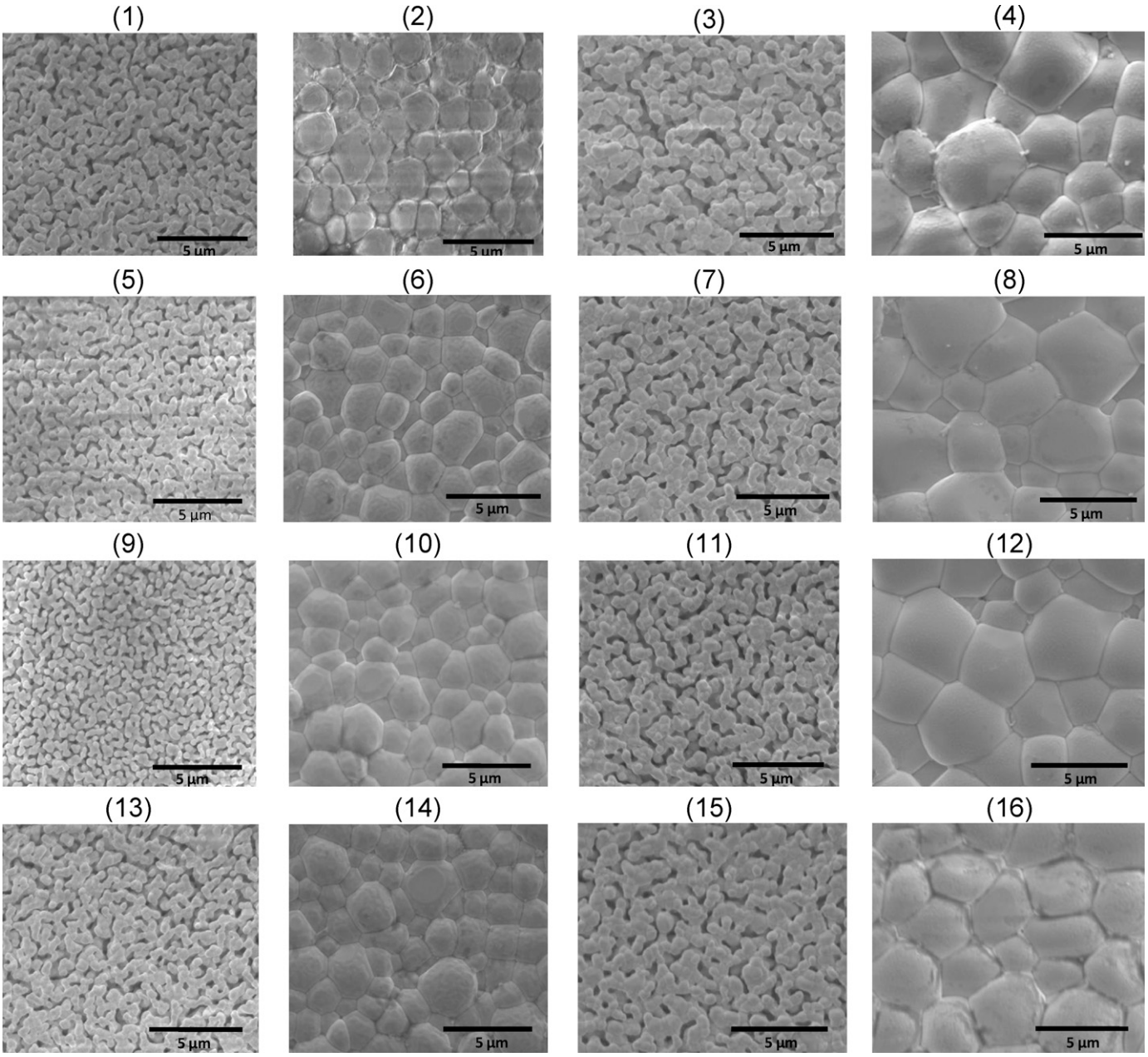

Fig. 1. SEM micrographs of the 2_V^{5-1} design for PLZT (9.5/65/35) ceramics sintered at various conditions. Refer to Table 1 for details.

influencing grain-growth were examined from the 2_V^{5-1} factorial design.

The grain diameters of the sintered ceramics range between 0.28 and 3.10 μm (Table 1). Based on the tabulated grain sizes, the factor's effects could be calculated, which in turn allow the construction of the residuals versus predicted, Pareto chart, and normal probability plot of residuals (Fig. 2). The residuals versus predicted plot shows that the variance increases with grain size, which is known as the constant percent error (Fig. 2a) [15]. The constant error problem is overcome by logarithmic transformation (Fig. 2b). The Pareto charts of *t*-value of |transformed grain size| show that D_1, sintering temperature (°C), is the most significant factor affecting grain size, followed by C_1, sintering time (h). Their interaction, C_1D_1, appears to be significant as well (Fig. 2c). The *t*-values of |transformed grain size| with respect to D_1, C_1, and C_1D_1 are above the *t*-value limit, as well as above the Bonferroni limit. The significant effect due to D_1, C_1, and C_1D_1 is confirmed by analysis of variance (ANOVA) of the $\log_{10}$ transformed response (Table 2). It is safe to ignore the aliasing, since a high level of interaction is involved [15]. The normal probability plot of residuals confirms that there is no problem with normality and severe outliers in the data (Fig. 2d).

The plot of significant main effects (C_1 and D_1) and interaction effects (C_1D_1) are depicted in Fig. 3a–c. Both C_1 and D_1 show positive effects on grain size, and the growth rate is greater at the higher sintering temperature, 1250 °C (Fig. 3c). The smallest grain-size was achieved for the short sintering

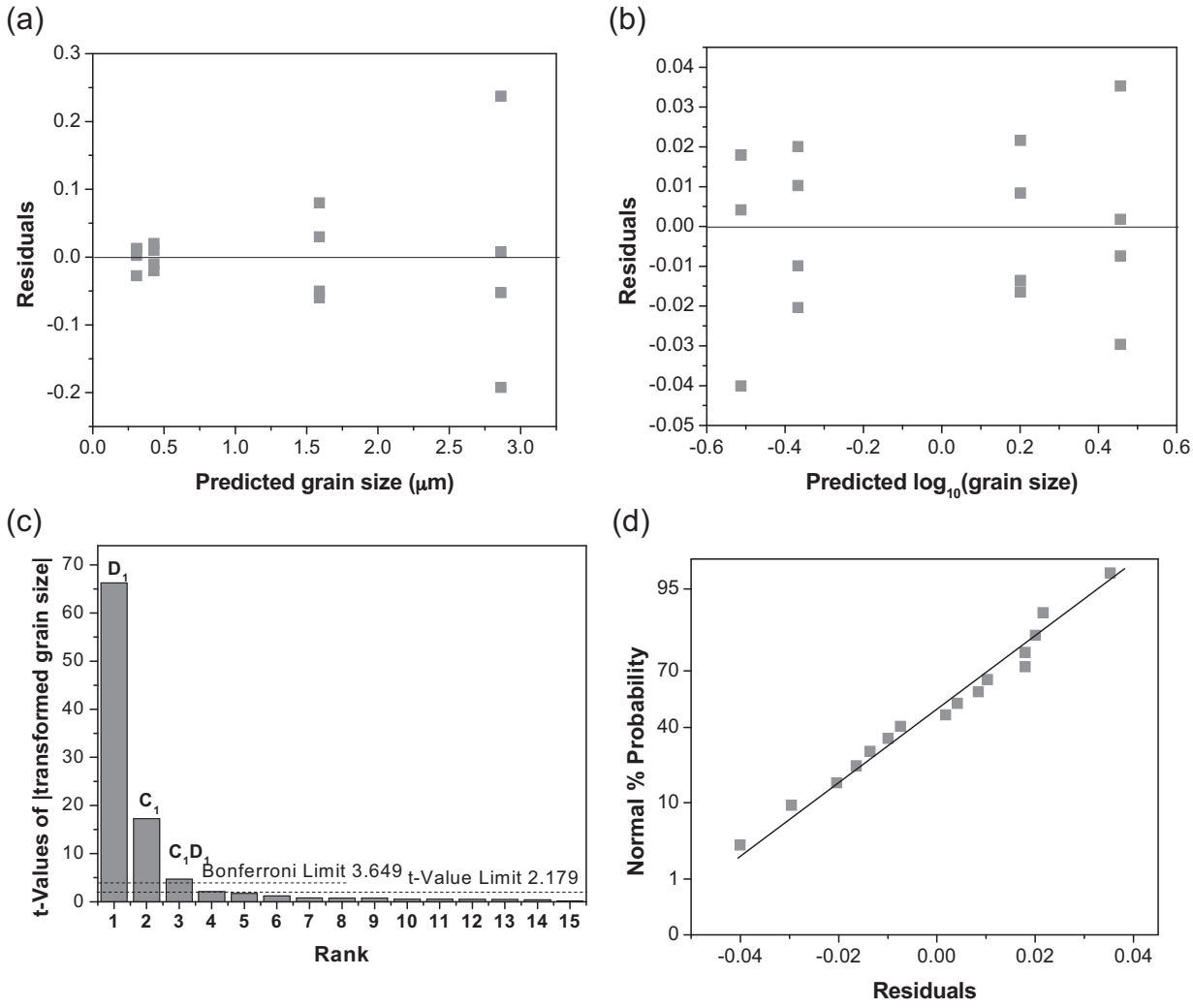

Fig. 2. (a) Plot of residuals versus predicted with grain size as the measured response. Plots of (b) residuals versus predicted, (c) Pareto chart of *t*-values of |transformed grain size|, and (d) normal probability plot of residuals with $\log_{10}$ (grain size) as the measured response.

time and low sintering temperature, Run no. 1-9 (C_1 = 2 h, D_1 = 1050 °C), and the largest grain-size was achieved for the long sintering time and high sintering temperature, Run no. 1-16 (C_1 = 12 h, D_1 = 1250 °C). At 1050 °C sintering temperature, the average grain sizes are below 0.5 μm and the ceramics are mainly populated with pores. Each grain has only undergone the initial sintering stage, as characterized by necked growth. In contrast, for the ceramics that were sintered at 1250 °C the average grain sizes are greater than 1.5 μm and they are closely packed. This is a further indication that the grain growth has reached the intermediate to final sintering stage. There is a stark difference in the ceramic qualities between those that were sintered at 1050 °C and those that were sintered at 1250 °C. The former samples are white in color, brittle, and opaque, while the latter samples are pale-yellow in color, translucent, and robust.

Breval et al. have reported the formation of a ZrO_2 impurity phase in a Zr-rich sintered PLZT when precaution against PbO evaporation is neglected during annealing in air [19]. The impurity peak which shows the highest intensity at $2\theta = 28.2^\circ$

Table 2
ANOVA with $\log_{10}$ (grain size) as the response variable for the 2_V^{5-1} design.

Source of variation	SS	df	MS (SS/df)	*F*-value	*P*-value
Model	2.535	3	0.845	1570.61	<0.0001
D_1: sintering temperature (°C)	2.362	1	2.362	4390.84	<0.0001
C_1: sintering time (h)	0.161	1	0.161	298.90	<0.0001
C_1D_1	0.012	1	0.012	22.10	0.0004
Residuals	6.455E−03	12	5.379E−04		
Total	2.541	15			

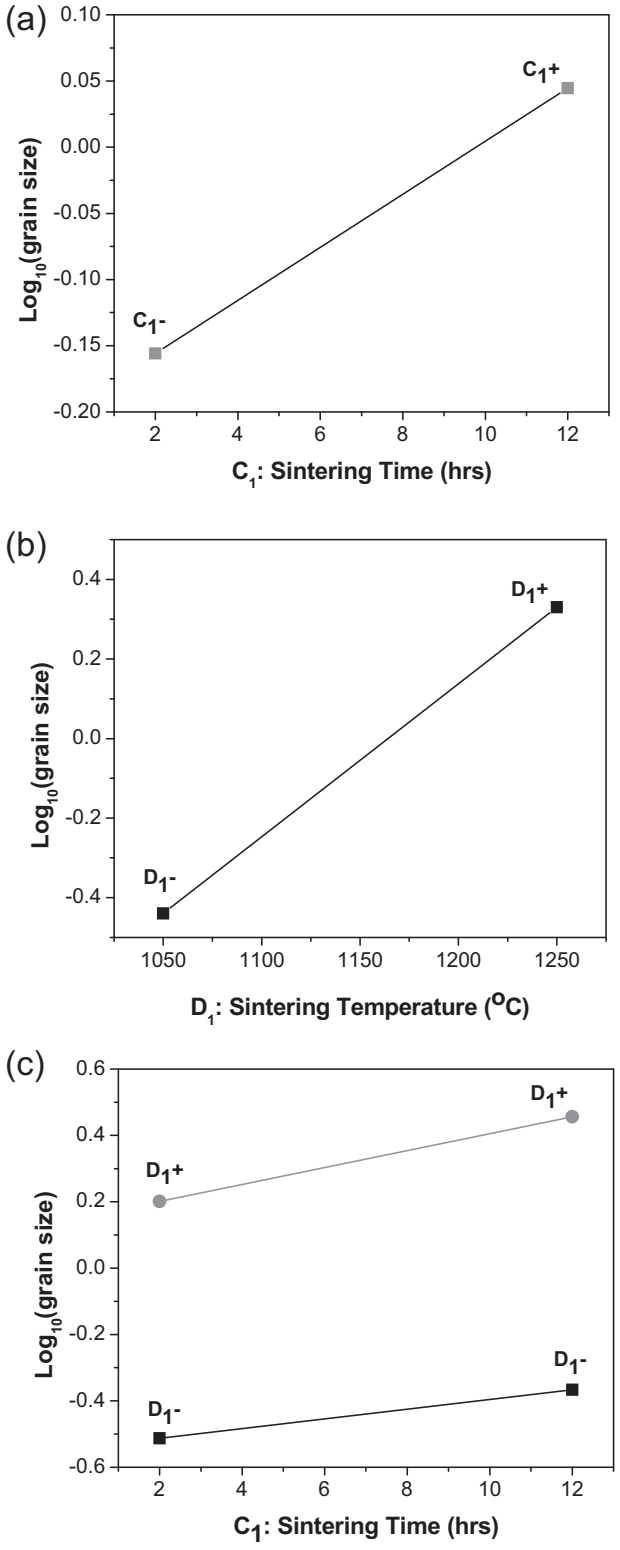

Fig. 3. Plots of main effect of factor (a) C_1: sintering time (h), (b) D_1: sintering temperature (°C) and (c) interaction C_1D_1: sintering time and sintering temperature for the 2_V^{5-1} design.

can be matched to PDF No. 01-078-0047, ZrO_2, rather than the usual pyrochlore phase, $La_2Zr_2O_7$ [6]. The pyrochlore phase is formed due to Pb deficiency, which is soluble in PLZT at a higher sintering temperature, whereas the ZrO_2 phase is formed due to disintegration of the perovskite PLZT. To compare the relative amounts of ZrO_2 impurity phases in each sample, the ratio of the highest intensity peaks due to ZrO_2 and due to PLZT, I_{ZrO_2}/I_{PLZT}, are tabulated (Table 1). The strongest peaks of PLZT and ZrO_2 occur at $2\theta = 31.4°$ and $2\theta = 28.2°$, respectively. Table 1 shows that the I_{ZrO_2}/I_{PLZT} ratios range from as low as 0.003 (0.3%, Run no. 1-3 and 1-11) to 0.02 (2%, Run no. 1-4), which suggest a modest amount of ZrO_2 impurity phase formation. Table 1 also shows that the ZrO_2 impurity phase is seen in all samples, even at 1050 °C sintering temperature, and the I_{ZrO_2}/I_{PLZT} ratio is generally higher for the higher sintering temperature (1250 °C) and the longer sintering time (12 h).

3.3. PLZT density

In order to examine the factors influencing the ceramic density and linear shrinkage, data for the ceramics that were sintered at 1050 °C were not accounted, which reduces the factorial design into 2_{IV}^{4-1} (see Table 3). $I = A_2B_2C_2D_2$ was used as the defining relation. The residuals versus predicted plot show a stable variance, so no data transformation is needed (Fig. 4a). The corresponding Pareto charts of t-value of |density| reveal that A_2: ball-milling time (h) and B_2: cold-press pressure (MPa) are the significant main effects, and no interaction effects are significant (Fig. 4b). Again, it is safe to ignore the aliasing effect, since a high level of interaction is involved [15]. The significant effects due to A_2 and B_2 are confirmed by analysis of variance (Table 4). The t-values of

Table 3
A 2_{IV}^{4-1} design for sintering of PLZT (9.5/65/35) ceramic. A_2 = ball-milling (h), B_2 = cold-press pressure (MPa), C_2 = sintering time (h), and D_2 = vacuum treatment (N/Y).

Run no.	A_2	B_2	C_2	D_2: $A_2B_2C_2$	ρ (g/cm^3)	Linear shrinkage (%)[a]
2-1	4	30	2	N	7.29 ± 0.04	31.1 ± 0.5
2-2	4	30	12	Y	7.37 ± 0.05	31.3 ± 2.1
2-3	4	240	2	Y	7.19 ± 0.08	25.0 ± 0.8
2-4	4	240	12	N	7.25 ± 0.06	25.9 ± 0.7
2-5	48	30	2	Y	7.55 ± 0.05	29.9 ± 0.7
2-6	48	30	12	N	7.56 ± 0.06	30.1 ± 0.6
2-7	48	240	2	N	7.49 ± 0.10	25.5 ± 0.5
2-8	48	240	12	Y	7.33 ± 0.10	25.3 ± 0.3

[a] Change in width dimension before and after sintering.

Table 4
ANOVA with density as the response variable for the 2_{IV}^{4-1} design.

Source of variation	SS	df	MS (SS/df)	F_0	P-value
Model	0.12	2	0.059	16.06	0.0067
A_2: ball-milling time (h)	0.086	1	0.086	23.32	0.0048
B_2: cold-press pressure (MPa)	0.033	1	0.033	8.81	0.0313
Residuals	0.018	5	3.693E−03		
Total	0.14	7			

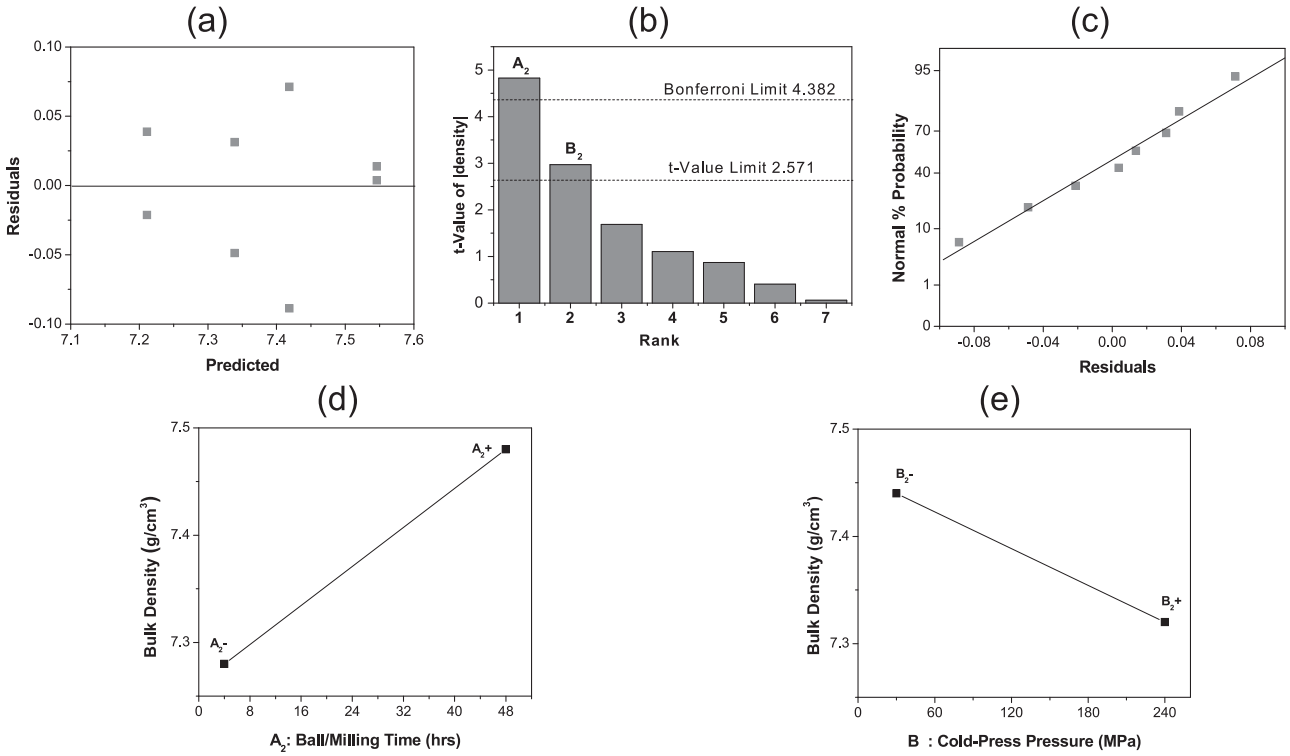

Fig. 4. Plots of (a) residuals versus predicted, (b) Pareto chart of *t*-values of |density|, and (c) normal probability plot of residuals with bulk density as the measured response for the 2_{IV}^{4-1} design. Main effect plots of (d) factor A_2: ball-milling time (h) and (e) B_2: cold-press pressure (MPa).

|density| with respect to A_2 and B_2 are above the *t*-value limit, but below the Bonferroni limit for B_2; which shows its inferior significance. The normal probability plot of residuals confirms that there is no problem with normality and severe outliers in the data (Fig. 4c).

The main factor plots show that A_2 has a positive effect, whereas B_2 has a negative effect on bulk density (Fig. 4d and e). High-density green bodies that contain fewer numbers of initial pores require less densification/shrinkage to obtain a final density with minimum defects. The long ball-milling time may have contributed to looser agglomerates, which improves the packing density of the green body [20]. In a highly packed green body each particle has a high coordination number with its neighbors, which facilitates neck growth during the initial sintering process. The higher cold-press pressure, on the other hand, may have contributed to packing defects which results in pore formation.

Table 1 shows that the relative amount of the ZrO_2 secondary phase is small with $I_{ZrO_2}/I_{PLZT} \leq 2\%$ and the maximum grain size is 3.1 μm for the 2_{IV}^{4-1} runs. The highest bulk density was determined to be 7.56 g/cm^3, Run no. 2-6 (Table 3), at the following sintering conditions: A_2: 48 h ball-milling, B_2: 30 MPa cold-press pressure, C_2: 2 h sintering, and D_2: no vacuum treatment.

3.4. Effect of PLZT to $PbZrO_3$ ratio on ceramic density

Subsequently, the influence of the $PbZrO_3$ to PLZT ratio and sintering time on the ceramics quality was examined with a 3^2 factorial experiments (Table 5). The formation of a high-density stoichiometric PLZT phase requires a sufficient PbO concentration in the atmosphere to ensure equilibrium between PbO in the sample and atmospheric PbO [12]. Table 5 shows that the relative I_{ZrO_2}/I_{PLZT} ratios generally increase with

Table 5
A 3^2 design for sintering of PLZT (9.5/65/35) ceramic. A_3 = sintering time (h) and B_3 = PLZT to $PbZrO_3$ weight ratio.

Run no.	A_3	B_3	ρ (g/cm^3)	Grain size (μm)	Linear shrinkage (%)	I_{ZrO_2}/I_{PLZT}
3-1	2	1:2	7.56 ± 0.07	1.53 ± 0.05	29.5 ± 0.5	0.010
3-2	2	1:4	7.55 ± 0.10	1.54 ± 0.10	29.9 ± 0.6	0.010
3-3	2	1:8	7.44 ± 0.05	1.65 ± 0.06	28.9 ± 0.7	0.010
3-4	7	1:2	7.57 ± 0.10	2.57 ± 0.27	29.7 ± 0.6	0.016
3-5	7	1:4	7.50 ± 0.03	2.62 ± 0.28	26.7 ± 0.3	0.016
3-6	7	1:8	7.52 ± 0.08	2.62 ± 0.30	29.3 ± 1.4	0.015
3-7	12	1:2	7.56 ± 0.06	2.81 ± 0.07	30.1 ± 0.6	0.011
3-8	12	1:4	7.49 ± 0.04	2.83 ± 0.10	30.2 ± 0.4	0.014
3-9	12	1:8	7.50 ± 0.06	2.97 ± 0.37	29.7 ± 0.4	0.016

Table 6
ANOVA with density as the response variable for the 3^2 design.

Source of variation	Sum of squares	df	MS	F_0	P-value
Model	0.01	4	2.36E−03	1.80	0.2915
A_3: sintering time (h)	3.56E−04	2	1.78E−04	0.14	0.8734
B_3: PLZT to $PbZrO_3$ ratio	9.09E−03	2	4.54E−03	3.47	0.1337
Residual	5.24E−03	4	1.31E−03		
Total	1.47E−02	8			

Table 7
ANOVA with grain size as the response variable for the 3^2 design.

Source of variation	Sum of squares	df	MS	F_0	P-value
Model	2.83	4	0.71	473.94	<0.0001
A_3: sintering time (h)	2.81	2	1.41	941.27	<0.0001
B_3: PLZT to $PbZrO_3$ ratio	0.02	2	9.88E−03	6.61	0.0540
Residual	0.01	4	1.49E−03		
Total	2.84	8			

increasing sintering time, but do not exceed 2%, which is consistent with the 2_V^{5-1} design for the fixed PLZT to $PbZrO_3$ ratios of 1:2. The fact that the amount of the impurity phase does not decline with increasing amounts of $PbZrO_3$, implies that the impurity phase is indeed not the Pb deficient pyrochlore phase (Table 5). ANOVA shows that neither the PLZT to $PbZrO_3$ ratio nor the sintering time has significant effects on the density variation (Table 6 and Fig. 5a). Moreover, the highest measured bulk density is close to that obtained from the 2_{IV}^{4-1} factorial experiment, 7.56 g/mL (Run no. 2-6) versus 7.57 g/mL (Run no. 3-4). Nonetheless, the 3^2 factorial experiments provide additional data for correlating the sintering time to grain size. The PLZT to $PbZrO_3$ weight ratio, however, shows no significant effect on the grain size (Table 7). The measured grain sizes across the different PLZT to $PbZrO_3$ ratios show overlapping least significant difference (LSD) intervals for $\alpha = 0.05$ (Fig. 5b). The grain size with respect to sintering time follows a power function, as reported by Duran and Moure [17].

Fig. 6a shows the typical X-ray diffraction pattern for the sintered PLZT 9.5/65/35, as well as its corresponding Raman spectrum (Fig. 6b). It can be indexed to a cubic crystal structure with a typical lattice parameter of $a \approx 4.08$–4.09 Å [21]. The optimum sintering conditions with respect to the various factors described in this work are summarized in Fig. 7, which is based on Run no. 3-4.

3.5. Properties of PLZT ceramics of the various compositions

In the final set of experiments, the optimized sintering conditions were used to fabricate PLZT ceramics with compositions 5/60/40, 5/54/46, and 5/40/60 according to the procedure summarized in Fig. 7. In addition, PLZT ceramics with composition 8/40/60 were prepared using PLZT powder purchased from Praxair, Inc. For a fixed amount of lanthanum dopant, increasing the amount of Ti content across the MPB

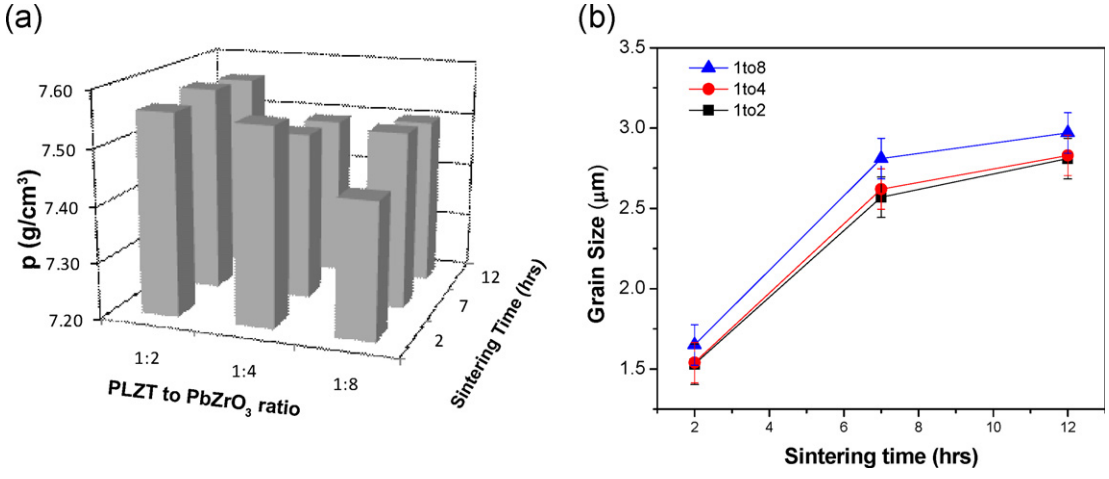

Fig. 5. (a) Plot of bulk density of PLZT (9.5/65/35) at various A_3: sintering time and B_3: PLZT to $PbZrO_3$ weight ratios, (b) plot of grain size versus sintering time.

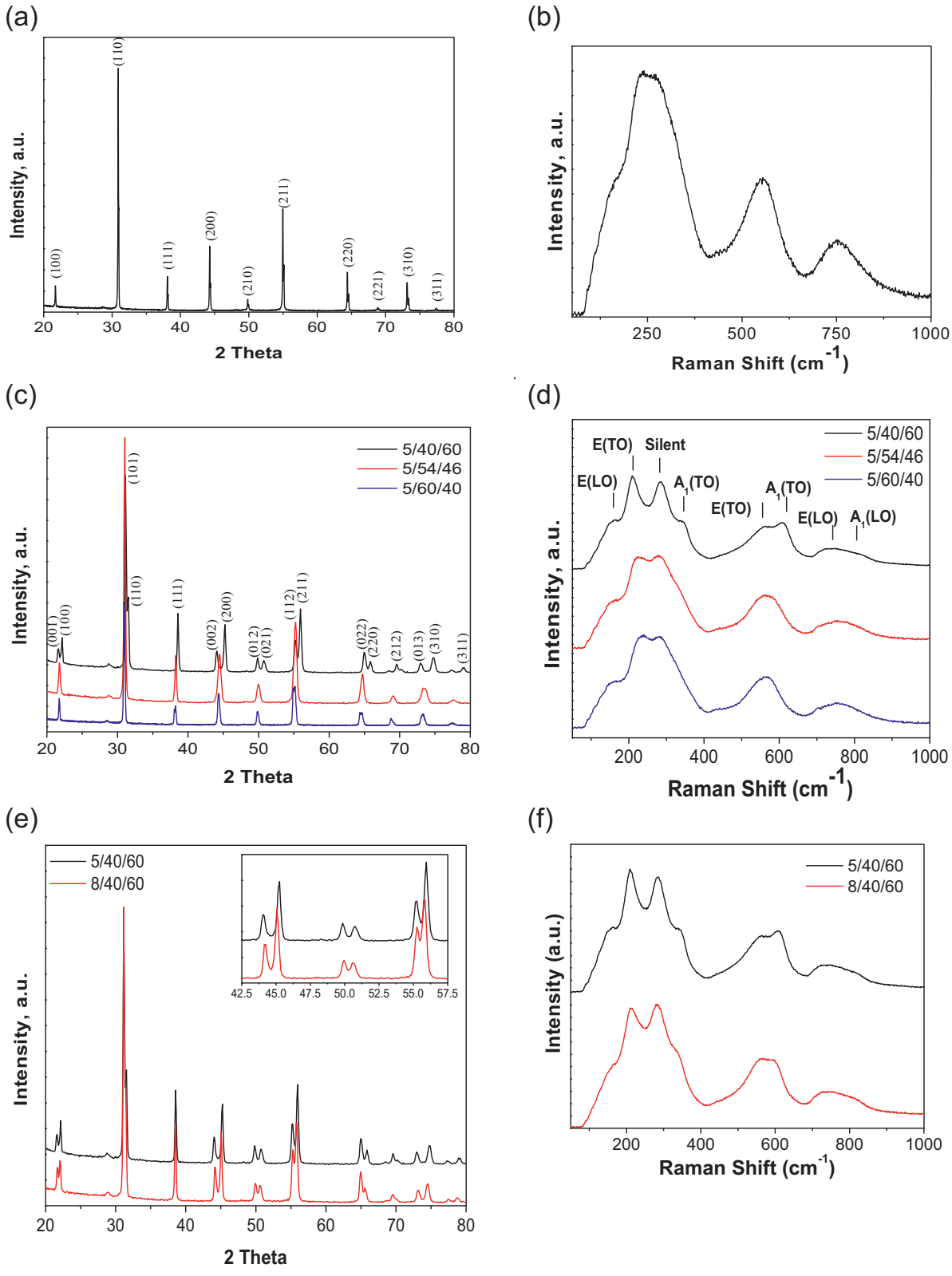

Fig. 6. (a and b) XRD and Raman spectra of sintered PLZT (9.5/65/35) ceramics. (c and d) XRD and Raman spectra of sintered PLZT ceramics at 5/Z/T compositions, Z/T = 40/60, 54/46, and 60/40. (e and f) XRD and Raman spectra of sintered PLZT ceramics at L/40/60 compositions, L = 5 and 8.

shifts the crystal structure from rhombohedral to tetragonal symmetry [22]. Near the MPB, the piezoelectric electromechanical coupling factors and the relative permittivity are highest for a given La content. At 5% La content, the 5/54/46 composition has been determined by Poosanaas and Uchino to display the optimum photostrictive effect [23].

Table 8 shows that the theoretical density of the coprecipitation oxide–alkoxide synthesized PLZT samples is

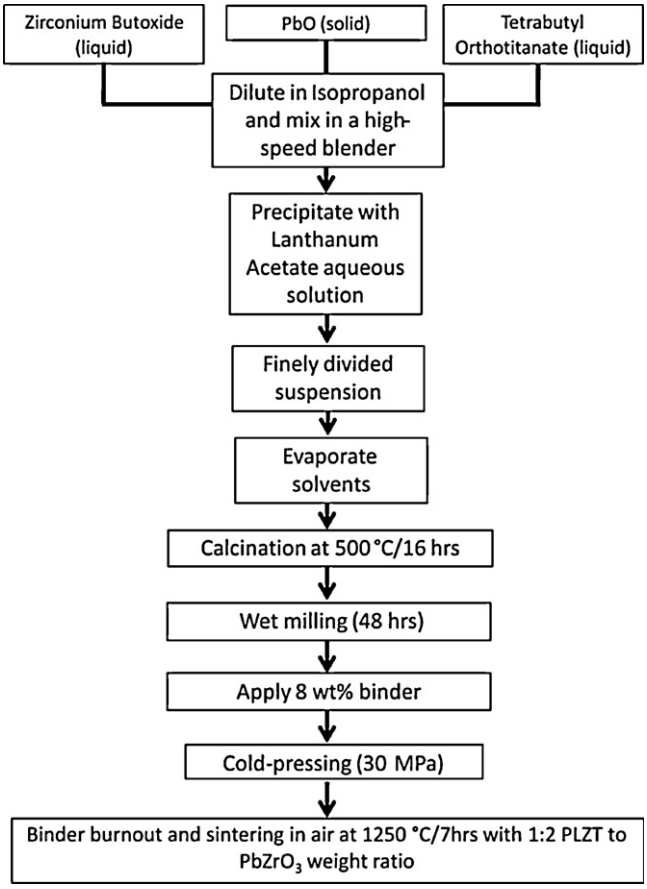

Fig. 7. Flow-chart for the coprecipitation oxide–alkoxide synthesis and subsequent fabrication of PLZT ceramics.

between 95% and 96%, and 97% for the commercially purchased PLZT (8/40/60) sample [1]. The latter sample showed only a 16% linear shrinkage compared with 29–30% for the coprecipitation oxide–alkoxide synthesized PLZT's because it did not require a binder for its green body fabrication. It is worth noting that the percent densification is dependent on the powder preparation techniques [13]. The influence of Zr/Ti ratios can be seen from the varying grain sizes amongst the 5/Z/T compositions. As previously reported in the literature, there is a positive correlation between Zr/Ti ratio and grain size (Table 8) [23]. Increasing the Zr content increases the grain size. For L/40/60 compositions, increasing the La content appears to increase the grain size as well (compare 5/40/60 with 8/40/60, Table 8). While the XRD spectra of L/40/60 (L = 5 and 8) can be unambiguously indexed with the tetragonal crystal structure, the XRD spectra of the 5/60/40 and 5/54/46 compositions are best indexed with the cubic crystal structure (Fig. 6c). Compared with the cubic crystal structure, the tetragonal crystal structure results in additional diffraction peaks that are attributed to the *c* axis in the [0 0 1] direction. The XRD spectra of the 5/60/40 and 5/54/46 compositions are indeed qualitatively similar to the XRD spectrum of the 9.5/65/35 composition (see Fig. 6c), except that the XRD peaks due to 5/60/40 and 5/54/46 compositions are wider, which may suggest a modestly distorted cubic structure, also known as pseudo-cubic – possibly rhombohedral or orthorhombic crystal structure. However, peak deconvolution is not able to conclusively fit an orthorhombic or a rhombohedral crystal structure. To simplify the determination of the lattice parameters, it may thus be treated as a cubic lattice [24]. All peaks in both XRD spectra can be fitted to the cubic crystal structure (Fig. 6c and Table 8).

The corresponding Raman spectra more clearly differentiate the crystal structures of the 9.5/65/35 composition from the 5/Z/T compositions (Z/T = 60/40 and 54/46), compare Fig. 6b with Fig. 6d [25]. For the 9.5/65/35 composition, the Raman spectrum shows mainly broad and featureless peaks which indicate a cubic phase [26,27]. The 5/Z/T (Z/T = 60/40 and 54/46) sample spectra on the other hand show distinct features within the 200–350 cm^{-1} region, suggesting a lower symmetry phase, which most likely indicates a rhombohedral phase [25]. The respective XRD and Raman spectra show only subtle differences in the spectra quality between the compositions 5/60/40 and 5/54/46.

The effect of varying the Zr/Ti ratios across the MPB for 5/Z/T compositions (Z/T = 60/40 and 54/46 versus 40/60) is corroborated in the Raman spectra (Fig. 6f). That is, additional peaks are seen for the 5/40/60 composition due to its lower symmetry (Fig. 6d), which resembles a tetragonal phase [26]. Since the peaks are resolved in a tetragonal phase PLZT, each peak can be assigned according to the single-crystal tetragonal $PbTiO_3$ (Fig. 6d) [28]. The peak splittings are less prominent in the higher symmetry PLZT samples with compositions 5/60/40 and 5/54/46, in particular in the high frequency range (500–900 cm^{-1}). In the low frequency range (200–400 cm^{-1}) the A_1(TO) mode, the *E*(TO) modes, and the silent modes are less resolved. Nevertheless, the peak splitting in the low frequency range in the 5/60/40 and 5/54/46 PLZT's suggests a rhombohedral/tetragonal mixed phase. Such a mixed phase is expected for PLZT compositions in the vicinity of the MPB. Fig. 6e shows that the tetragonality in PLZT L/40/60 is decreased with an increased amount of La. Fig. 6e inset shows that the extent of the XRD peak

Table 8
Measured responses for sintered PLZT pellets of various compositions.

L/Z/T	Lattice parameters (crystal structure)[a]	I_{ZrO_2}/I_{PLZT}	Shrinkage (%)	$\rho_{exp.}$ (g/cm^3) (% theoretical)	Grain size (μm)	ε_r	d_{33} ($\times 10^{-12}$ C/N)
9.5/65/35	a = 4.082 Å (C)	0.016	29.5 ± 0.1	7.57 (95%)	2.57 ± 0.27	4030	0
5/60/40	a = 4.083 Å (C)	0.018	29.0 ± 0.7	7.67 (96%)	1.48 ± 0.02	1250	199
5/54/46	a = 4.078 Å (C)	0.021	29.0 ± 0.3	7.54 (95%)	1.37 ± 0.03	2213	492
5/40/60	a = 4.00 Å, c = 4.11 Å (T)	0.024	28.8 ± 0.5	7.64 (96%)	1.14 ± 0.08	673	111
8/40/60	a = 4.024 Å, c = 4.10 Å (T)	0.023	16.0 ± 0.1	7.61 (97%)	1.52 ± 0.07	850	85

[a] C, cubic; T, tetragonal.

splitting is slightly more pronounced in 5/40/60, which corresponds to the higher *c*/*a* ratio than it is in 8/40/60. The *c*/*a* ratio is 1.028 for 5/40/60 and it is 1.019 for 8/40/60. In parallel, the corresponding Raman spectra show relatively less resolved peaks for PLZT 8/40/60 both in the low- (200–400 cm^{-1}) and the high-frequency (500–900 cm^{-1}) regions.

Table 8 lists the measured relative permittivity ε_r and the piezoelectric constant d_{33} for the various PLZT sample compositions. The highest relative permittivity, $\varepsilon_r = 4030$, is seen for the 9.5/65/35 composition, which is comparable with that reported in the literature [1]. The non-zero d_{33} values indicate that ferroelectricity is seen in all compositions, except for the 9.5/65/35 composition which has been reported to favor a relaxor behavior. An L/65/35 composition gradually undergoes a ferroelectric/ piezoelectric (FE) to relaxor/electrostrictive (R) transition with increasing lanthanum composition. The FE–R transition is accompanied with lowering of the Curie temperature which leads to a high dielectric and electrooptic properties at room temperature [29]. Amongst the 5/Z/T compositions (Z/T = 60/40 and 54/46 versus 40/60) both ε_r and d_{33} are highest for Z/T = 54/46 at the MPB, 2213 and 492×10^{-12} C/N, respectively. Beyond the MPB, the higher Zr/Ti ratio exhibits smaller ε_r and d_{33} constants. The measured values are in par with those reported by Poosanaas et al. for similar compositions [23]. Increasing the La content from 5% to 8% for the L/40/60 shows that the 8/40/60 composition remains ferroelectric with nonzero, but decreased d_{33} value with simultaneous increase in the ε_r value. The FE–R transition in L/40/60 composition has been reported to occur beyond L = 8 [28].

4. Conclusions

We have utilized factorial screening to determine the relevant factors affecting the quality of pressureless air-sintered PLZT ceramics. A mainly single perovskite-phase with low amounts of a ZrO_2 secondary phase ($I_{ZrO_2}/I_{PLZT} < 2\%$), a grain size of less than about 3.1 μm, and up to 96% bulk density was obtained by sintering PLZT powder that was prepared via the oxide–alkoxide coprecipitation process. The optimized sintering conditions (48 h ball milling time, 30 MPa cold-press pressure, 7 h sintering time, 1250 °C sintering temperature, 1:2 ratio of PLZT to $PbZrO_3$, and no vacuum treatment) were applied to other compositions, 5/Z/T (Z/T = 60/40, 54/46, and 40/60), as well as to a commercially purchased PLZT powder with composition 8/40/60 (Praxair, Inc.) to yield similar quality samples. These compositions lie across the morphotropic phase boundary. Ferroelectricity was observed in all samples, except for the 9.5/65/35 composition. Raman spectra confirmed the expected phonon structures. The described method is low-cost and requires a minimal setup compared with the well-known pressure-assisted sintering in oxygen-rich atmosphere.

Acknowledgement

This work was supported by ONR grants N00014-04-1-0688 and N00014-06-1-0315.

References

[1] G.H. Haertling, Ferroelectric ceramics: history and technology, J. Am. Ceram. Soc. 82 (4) (1999) 797–818.
[2] I.A. Santos, C. Endo, A.L. Zanin, M.H. Lente, J.A. Eiras, D. Garcia, Hot-pressed transparent PLZT ceramics from low cost chemical processing, Mater. Res. 4 (4) (2001) 291–295.
[3] G.S. Snow, Fabrication of transparent electrooptic PLZT ceramics by atmospheric sintering, J. Am. Ceram. Soc. 56 (2) (1973) 91–96.
[4] J.J. Choi, J. Ryu, H.E. Kim, Microstructural evolution of transparent PLZT ceramics sintered in air and oxygen atmospheres, J. Am. Ceram. Soc. 84 (7) (2001) 1465–1469.
[5] P. Poosanaas, A. Dogan, S. Thakoor, K. Uchino, Influence of sample thickness on the performance of photostrictive ceramics, J. Appl. Phys. 84 (3) (1998) 1508–1512.
[6] E. Breval, M. Klimkiewicz, C.P. Wang, J.P. Dougherty, A. Crespi, Sinterability and decomposition of $Pb_{0.9175}La_{0.055}Zr_{0.975}Ti_{0.025}O_3$: influence of calcination and sintering temperature, J. Am. Ceram. Soc. 90 (7) (2007) 2043–2049.
[7] P. Sun, C.N. Xu, M. Akiyama, T. Watanabe, Controlled oxygen partial pressure sintering of (Pb,La)(Zr,Ti)O-3 ceramics, J. Am. Ceram. Soc. 82 (6) (1999) 1447–1450.
[8] A.R. James, J. Subrahmanyam, K.L. Yadav, Structural and electrical properties of nanocrystalline PLZT ceramics synthesized via mechano-chemical processing, J. Phys. D: Appl. Phys. 39 (10) (2006) 2259–2263.
[9] S. Roy, S. Bysakh, M.L.N. Goswami, D. Jana, J. Subrahmanyam, Single-step synthesis of ultrafine PLZT from polymer gel precursor: synthesis, consolidation, and dielectric properties, Chem. Mater. 19 (10) (2007) 2622–2629.
[10] L.B. Kong, J. Ma, H. Huang, R.F. Zhang, Effect of excess PbO on microstructure and electrical properties of PLZT 7/60/40 ceramics derived from a high-energy ball milling process, J. Alloys Compd. 345 (1–2) (2002) 238–245.
[11] E. Breval, C. Wang, J.P. Dougherty, K.W. Gachigi, PUT phases near lead zirconate: 1. Determination by X-ray diffraction, J. Am. Ceram. Soc. 88 (2) (2005) 437–442.
[12] M. Cerqueira, R.S. Nasar, E.R. Leite, E. Longo, J.A. Varela, Sintering and characterization of PLZT (9/65/35), Ceram. Int. 26 (3) (2000) 231–236.
[13] P. Poosanaas, A. Dogan, A.V. Prasadarao, S. Komarneni, K. Uchino, Effect of ceramic processing methods on photostrictive ceramics, Adv. Perform. Mater. 6 (1) (1999) 57–69.
[14] G.H. Haertling, C.E. Land, Recent improvements in the optical and electrooptic properties of PLZT ceramics, Ferroelectrics 3 (1972) 269–280.
[15] D.C. Montgomery, Design and Analysis of Experiments, 5th ed., John Wiley, New York, 2001.
[16] M.J. Anderson, P.J. Whitcomb, DOE Simplified: Practical Tools for Effective Experimentation, 2nd ed., Productivity Press, New York, 2007 .
[17] P. Duran, C. Moure, Sintering at near theoretical density and properties of PZT ceramics chemically prepared, J. Mater. Sci. 20 (3) (1985) 827–833.
[18] T.A. Ring, Fundamentals of Ceramic Powder Processing and Synthesis, Academic Press, San Diego, 1996.
[19] E. Breval, M. Klimkiewicz, C. Wang, J.P. Dougherty, A. Crespi, Annealing of sintered $Pb_{0.9175}La_{0.055}Zr_{0.975}Ti_{0.025}O_3$ in air, J. Am. Ceram. Soc. 90 (8) (2007) 2664–2666.
[20] R.M. German, Sintering Theory and Practice, Wiley Interscience, New York, 1996.
[21] B.D. Stojanovic, M.A. Zaghete, C.O. Paiva-Santos, M. Cilense, R. Magnani, E. Longo, J.A. Varela, Hot-pressed 9.5/65/35 PLZT prepared by the polymeric precursor method, Ceram. Int. 26 (6) (2000) 625–630.
[22] N.W. Thomas, Crystal structure–physical property relationships in perovskites, Acta Crystallogr. B 45 (1989) 337–344.
[23] P. Poosanaas, K. Uchino, Photostrictive effect in lanthanum-modified lead zirconate titanate ceramics near the morphotropic phase boundary, Mater. Chem. Phys. 61 (1) (1999) 36–41.

[24] L. Karmazin, W.J. James, Precise measurement of lattice parameters of pseudocubic lattices, Acta Crystallogr. A 28 (1972) 183–187.
[25] V.V. Efimov, E.A. Efimova, S.S. Khasanov, Y.S. Kovalev, B.N. Mavrin, A.O. Pogosov, A. Sternberg, S.I. Tiutiunikov, Mechanism of pulsed electron irradiation of the PLZT *X*/65/35 ceramics, Phys. Status Solidi (c) 2 (1) (2005) 449–452.
[26] E. Buixaderas, I. Gregora, S. Kamba, J. Petzelt, M. Kosec, Raman spectroscopy and effective dielectric function in PLZT *x*/40/60, J. Phys.: Condens. Matter 20 (34) (2008), 345229/345221–345229/345210.
[27] J.L. Dellis, J. Dallennes, J.L. Carpentier, A. Morell, R. Farhi, A Raman and dielectric susceptibility study of superparaelectric PLZT ceramics, J. Phys.: Condens. Matter 6 (27) (1994) 5161–5168.
[28] A. Lurio, G. Burns, Vibrational modes in (Pb,La)(Zr,Ti)O_3 ceramics, J. Appl. Phys. 45 (5) (1974) 1986–1992.
[29] A.L. Kholkin, D.A. Kiselev, I.K. Bdikin, A. Sternberg, B. Dkhil, S. Jesse, O. Ovchinnikov, S.V. Kalinin, Mapping disorder in polychrystalline relaxors: a piezoresponse force microscopy approach, Materials 3 (2010) 4860–4870.